

Tunable Bipolar Photothermoelectric Response from Mott Activation for In-Sensor Image Preprocessing

Bowen Li, Ning Lin, Zhaowu Wang, Baojie Chen, Changyong Lan, Xiaocui Li, You Meng, Weijun Wang, Mingqi Ding, Pengshan Xie, Yuxuan Zhang, Zenghui Wu, Dengji Li, Fu-Rong Chen, Chi Hou Chan, Zhongrui Wang,* and Johnny C. Ho*

In-sensor image preprocessing, a subset of edge computing, offers a solution to mitigate frequent analog-digital conversions and the von Neumann bottleneck in conventional digital hardware. However, an efficient in-sensor device array with large-scale integration capability for high-density and low-power sensory processing is still lacking and highly desirable. This work introduces an adjustable broadband photothermoelectric detector based on a phase-change vanadium dioxide thin-film transistor. This transistor employs a vanadium dioxide/gallium nitride three-terminal structure with a gate-tunable phase transition at the gate-source junctions. This design allows for modulable photothermoelectric responsivities and alteration of the short-circuit photocurrent's polarities. The devices exhibit linear gate dependence for the broadband photoresponse and linear light-intensity dependence for both positive and negative photoresponsivities. The device's energy consumption is as low as 8 pJ per spike, which is one order of magnitude lower than that of previous Mott materials-based in-sensor preprocessing devices. A wafer-scale bipolar phototransistor array has also been fabricated by standard micro-/nano-fabrication techniques, exhibiting excellent stability and endurance (over 5000 cycles). More importantly, an integrated in-sensor convolutional network is successfully designed for simultaneous broadband image classification, medical image denoising, and retinal vessel segmentation, delivering exceptional performance and paving the way for future smart edge sensors.

1. Introduction

Edge computing is gaining prominence due to the proliferation of smart cameras, watches, glasses, and earbuds, which collectively drive the rapid advancement of Internet of Things (IoT) technologies.^[1–5] Nevertheless, the considerable real-time data produced by these IoT sensors frequently necessitates transfer to computing units employing von Neumann architecture. This data transfer incurs substantial data movement to processing units, resulting in high energy consumption and latency overhead.^[6–9] Conversely, human vision's capacity for concurrent sensing, memory, and low-level signal processing enables the efficient execution of complex image tasks in real-time, diminishing power consumption and latency. This strategy could yield significant advantages for intelligent edge devices.^[10–14] For instance, advances in 2D materials have led to successes in in-sensor or near-sensor dynamic computing, in which simultaneous broadband image sensing and convolutional processing were achieved in 2D heterojunction photodetectors by the

B. Li, X. Li, Y. Meng, W. Wang, M. Ding, P. Xie, Y. Zhang, Z. Wu, D. Li, F.-R. Chen, J. C. Ho
 Department of Materials Science and Engineering
 City University of Hong Kong
 Hong Kong SAR 999077, P. R. China
 E-mail: johnnyho@cityu.edu.hk

B. Li, F.-R. Chen, J. C. Ho
 Shenzhen Research Institute
 City University of Hong Kong
 Shenzhen 518057, P. R. China

B. Li, B. Chen, C. H. Chan, J. C. Ho
 State Key Laboratory of Terahertz and Millimeter Waves
 City University of Hong Kong
 Hong Kong SAR 999077, P. R. China

N. Lin, Z. Wang
 Department of Electrical and Electronic Engineering
 The University of Hong Kong
 Hong Kong SAR 999077, P. R. China
 E-mail: zrwang@eee.hku.hk

Z. Wang
 School of Science
 Hebei University of Technology
 Tianjin 300401, P. R. China

 The ORCID identification number(s) for the author(s) of this article can be found under <https://doi.org/10.1002/adma.202502915>

DOI: 10.1002/adma.202502915

electrically tunable band structures.^[15–19] However, the operative voltages of these devices are excessively high, which can be energy-consuming for large-scale IoT applications.^[20] Moreover, since the photoresponse of these heterogenous devices is sensitive to the growth conditions, interface contacts, layer thickness, and even the measurement environment, scaling up these technologies with mainstream IC manufacturing processes will be challenging.^[21–23] Alternatively, the phase-change heterostructure devices based on Mott materials offer the ability to fabricate low-power, large-scale neuromorphic electronic and optoelectronic devices that have already been demonstrated.^[24–26] However, the characteristics of broadband spectrum responsiveness and adjustable positive and negative photoresponsivity in these devices are still absent, which produces great obstacles for high-density and energy-efficient in-sensor image preprocessing (ISIP) applications due to the need for the same physical processes in broadband sensing and convolutional computing.

On the other hand, vanadium dioxide (VO₂), a classic Mott material, undergoes a unique phase transition from the monoclinic insulating phase to the rutile metallic phase under external stimuli such as temperature, electric field, and laser irradiation near room temperature.^[27,28] This phase transition significantly changes VO₂'s optical, electrical, thermal, and magnetic properties.^[29,30] These properties are now being leveraged for various applications, including smart windows,^[31,32] radiative cooling coatings,^[33] infrared detection bolometers,^[34] self-adaptive metasurfaces,^[35] and thermal memristor devices.^[36] While an enhanced photothermoelectric (PTE) device leveraging this phase transition has been reported,^[37] the dynamic interplay between phase transition and PTE effect in VO₂ remains unexplored. This unexplored area presents an opportunity for adjustable broadband PTE detection. Furthermore, the dynamic phase-change regulation at the interface of VO₂ heterostructures can be gate-tunable, paving the way for novel electronic and optoelectronic devices that extend beyond traditional complementary metal-oxide-semiconductor systems.^[38–43] Examples include hybrid-phase-transition field-effect transistors,^[38,40] infrared-sensitive avalanche photodetectors,^[41] and electric-double-layer Mott transistors with ionic liquid.^[42,43] These findings suggest the potential for achieving ISIP with VO₂-based phase transformation heterostructures by exploring broadband and gate-tunable PTE photoresponses and wafer-scale array fabrication. Additionally, broadband ISIP devices with tunable bipolar responses can complement bio-inspired artificial eye designs by providing adaptive light perception in dynamic environments, similar to retinal ganglion cells.^[44]

In this article, we introduce a three-terminal PTE detector using VO₂/GaN thin-film heterostructures. By artificially regulating the width of the space-charge region near the source and controlling the phase transition of VO₂ with different polarity gate voltages, we can alter the local phase distribution and adjust the PTE performance of the VO₂ channel near source regions. This adjustable PTE performance near the source can disrupt the symmetry of the electric potential in the heterostructure devices, resulting in a broadband linear gate-dependent photoresponsivity and a gate-tunable positive and negative photoresponse, which physically implements convolution with ultralow energy consumption of 8 pJ per spike. We successfully realized a wafer-scale PTE device array with integrated sensing in VO₂ grown on a GaN/Al₂O₃ substrate. Furthermore, we demonstrated exceptional performance in hyperspectral image classification using in-sensor computing based on the VO₂ technotrons. The Mott activation in-sensor dynamic processing proved highly accurate and energy-efficient in complex medical image denoising and retinal vessel segmentation, yielding results nearly identical to those obtained from state-of-the-art software convolutional models.

2. Results and Discussion

2.1. Device Fabrication and Bipolar Photocurrent Behaviors

The device fabrication began with the epitaxial growth of high-quality VO₂ films on a p-type GaN (001) crystal surface using a plasma-enhanced RF magnetron sputtering system. Standard microfabrication processes were then employed to create the source, drain, and gate electrodes. To ensure optimal ohmic contact and adhesion, Au/Ti was chosen as the electrode material prepared by e-beam evaporation (Figure S1, Supporting Information). In the Mott technotrons, an n-type VO₂ channel layer forms a p-n junction with p-GaN, generating a space-charge region modulated by the gate voltage, inducing a local phase transition of the VO₂ layer near the source region as illustrated in Figure 1a. The cross-sectional TEM and corresponding energy dispersive spectroscopy (EDS) images (Figure 1b,c) display the clear VO₂/GaN thin-film heterostructure and its evenly distributed constituent elements. Further device characterization was conducted using an X-ray diffractometer to analyze the out-of-plane growth behavior of the VO₂ thin film on a p-GaN/Al₂O₃ substrate. As reported previously,^[45] the peak located at $2\theta = 39.8^\circ$ is attributed to VO₂ (020) or (002) diffraction, while the 2θ peak at 34.72° and 41.68° are from the GaN (002) and Al₂O₃ (006) layers, respectively (Figure S2a, Supporting Information), which demonstrates the highly oriented growth of the VO₂ epitaxial film. Interestingly, we find that the peak position of the 20 nm VO₂ film shifts to a lower 2θ value of 39.6° , while the peaks of the 4-nm and 40-nm VO₂ films are at 39.3° and 39.8° , respectively, indicating that the modulation difference for the phase transformation of VO₂ film with different thickness is limited by the width of the intrinsic space-charge region in the VO₂/GaN heterojunction (Figure S2b, Supporting Information). The spherical aberration-corrected high-resolution transmission electron microscopy (ACTEM) also visualized the epitaxial growth of VO₂ (100)_R films on GaN (0001) crystal layers and two types of VO₂ domains (4–6 nm dimension) parallel to the GaN [0-11-1] direc-

Z. Wang
National Laboratory of Solid State Microstructures
Nanjing University
Nanjing 210093, P. R. China

B. Chen, C. H. Chan
Department of Electrical Engineering
City University of Hong Kong
Hong Kong SAR 999077, P. R. China

C. Lan
State Key Laboratory of Electronic Thin Films and Integrated Devices
University of Electronic Science and Technology of China
Chengdu 610054, P. R. China

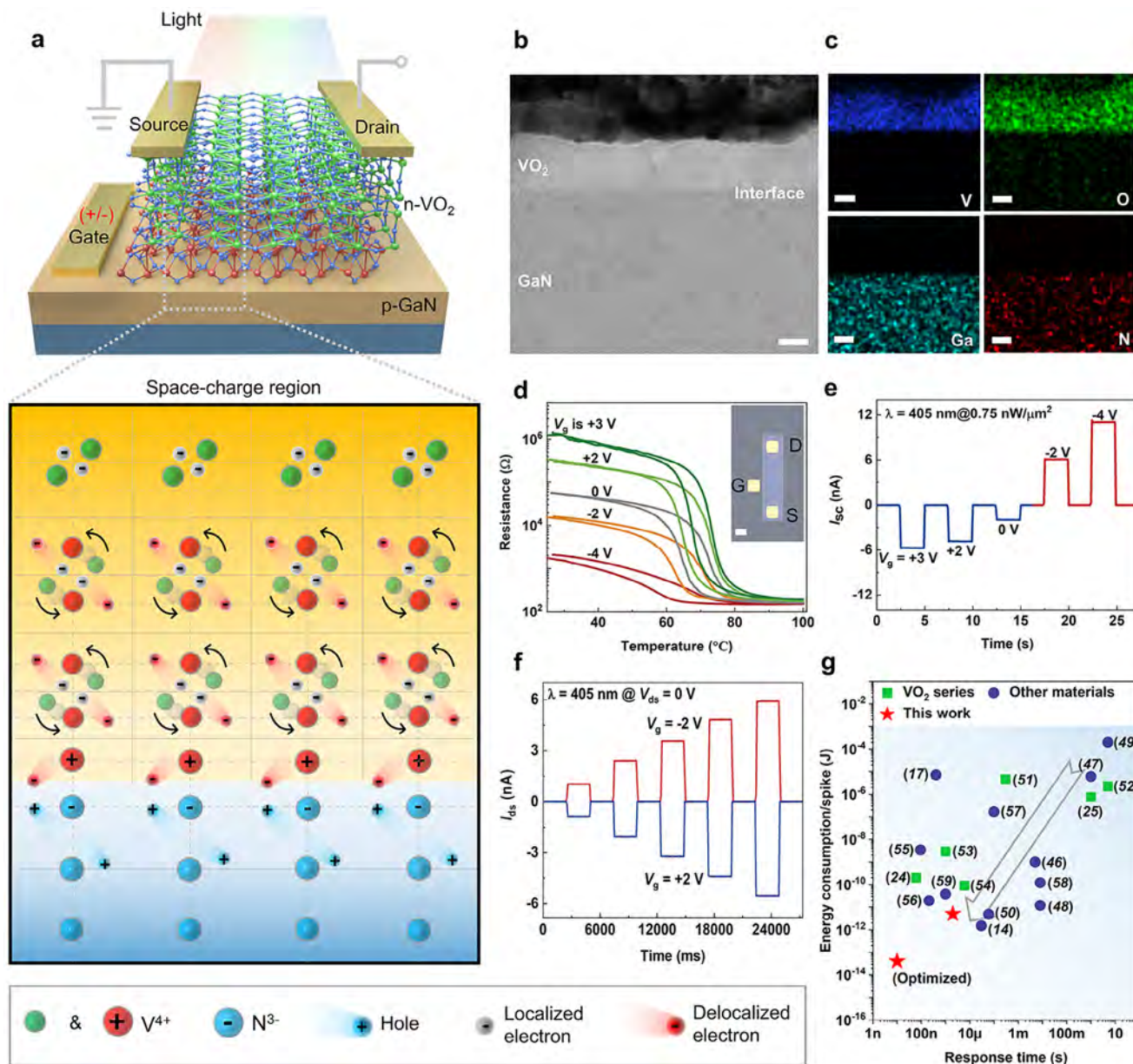


Figure 1. Device characterization of the three-terminal VO₂/GaN heterostructure detectors. a) The schematic of the PTE device with n-VO₂ film epitaxial growth on the p-GaN layer to form a p-n junction, source and drain electrodes are set on the VO₂ surface, and the gate electrode is on the GaN surface. The local magnification diagram explains that the space-charge region can be regulated by the gate voltage, causing the localized electrons of VO₂ to be delocalized to maintain the dynamic balance of junction carriers (hole and electron), finally resulting in a positive or negative PTE response under light illumination. Green & red sphere, positive tetravalent V ion, and blue sphere, positive trivalent N ion. b) Cross-sectional TEM image of the heterostructure constructed by VO₂ and GaN film layers. c) EDS maps of VO₂ and GaN layers (b), respectively. All scale bars are 10 nm. d) Resistance-temperature curves of the VO₂ channel regulated by the gate voltage range from +3 V to -4 V when the source-drain voltage of 0.5 V is applied. The illustration presents an optical image of the actual device. Scale bar, 50 μm . e) Time-resolved short-circuit photocurrent response of (d): negative and positive currents without applied source-drain voltage ($V_{ds} = 0\text{ V}$, $\lambda = 405\text{ nm}$). f) Response relationship of negative and positive I_{sc} with laser irradiation power ranging from 0.06 to 0.73 $\text{nW}\ \mu\text{m}^{-2}$ under the gate voltages of +2 and -2 V, respectively. g) Power consumption summary of recent comparable ISIP devices.

tion, demonstrating the atom-matching crystallinity of the heterogeneous VO₂/GaN interface (Figure S3, Supporting Information). Near-perfect heterogeneous interfaces exhibit higher mobility due to the negligible defects.^[46] Additional characterization of the phase and chemical composition of these VO₂ film samples was carried out with Raman and XPS instruments (Figures

S4 and S5, Supporting Information). Further details on device fabrication and characterization can be found in the Experimental section.

Figure 1d shows the dynamic resistance-temperature characteristics of the VO₂ channel layer in our PTE device. As demonstrated above, the initial resistance of the 20-nm VO₂ channel is

in the middle state at room temperature due to dynamic charge injection originating from the intrinsic depletion region in the VO₂/GaN p-n junction. When the gate voltage is set to +3 V, the space-charge region narrows, resulting in more VO₂ converting to an insulating state, and the resistance of the VO₂ channel increases to a more insulated state. However, when the gate voltage is set to -4 V, the space-charge region widens, causing more of the VO₂ to convert to a metallic state, and the resistance of the VO₂ channel continues to decrease to a more metallic state. Correspondingly, the time-resolved photocurrent characteristics of the VO₂ PTE detector are shown in Figure 1e. The PTE detector exhibits a negative photocurrent with a positive gate voltage. In contrast, when the negative gate voltage is applied, the PTE detector exhibits a positive photocurrent. This gate-tunable bipolar photoresponsivity is desirable for ISIP. In Figure 1f, the dynamic photocurrent further demonstrates its tunable polarities under the gate voltage with different polarities and values, which also shows a linear photoresponsivity with the irradiation power ranging from 0.06 to 0.73 nW μm⁻² of the 405 nm laser. Furthermore, the response speeds of the positive and negative PTE effects under illumination at a wavelength of 405 nm were measured via a phase-locked amplification technique. Both rising and falling times for the positive or negative photoresponse are in the range of 1.7–3.7 μs, including other illumination wavelengths at 365, 532, and 808 nm (Figure S6, Supporting Information), which shows well co-frequency and broadband detection potential for ISIP, as well as the lower parasitic photomemory effect that is another requirement for constructing fast broadband image sensors. In addition to being able to possess important ISIP functions, an ideal edge vision sensor should also achieve fast response speed and low energy consumption for a light spike, so we summarized the recent data regarding the response times and energy consumption of ISIP devices based on VO₂ and other 2D materials.^[14,17,24–25,47–60] As shown in Figure 1g, based on our device structure's unique design, our device's lowest energy consumption is as minimal as ≈8 pJ per spike. By contrast, the energy consumption is an order of magnitude lower than that of the previous VO₂-based ISIP devices. It is on par with other 2D materials-based devices, offering a new hardware solution for battery-powered and high-speed issues in edge analog computing. If we further consider the ultrafast phase transition potential of VO₂, we can get an optimized minimum energy equal to ≈40 fJ based on the previous research.^[24,61] It should be noted that here, we only consider the dynamic energy consumption of a single pixel when the photodetector is excited about each exposure (Further explanations can be found in Note S1, Supporting Information).

2.2. Gate-Tunable Photocurrent Characteristics

The gate-tunable photocurrent characteristics of the PTE device were studied using a three-terminal JFET configuration, with source and drain electrodes deposited on the VO₂ surface and the gate on the GaN surface. We collected multiple self-powered photocurrent states (I_{sc}) by applying a stationary light intensity under short-circuit conditions. To investigate the tunable polarity and strength of the photocurrent, we conducted photocurrent map-

ping measurements by scanning the laser spot across the drain, channel, and source (Figure 2a–c). As shown in Figure 2b(i,ii), the photoresponse, without applying the gate voltage, was locally observed at the metal-VO₂ contact (dashed square) with a similar strength but opposite signs, where the drain photocurrent was negative. In contrast, the photocurrent at the source was positive. However, by applying a gate voltage of +2 V, the same device showed a significantly reduced positive photocurrent at the source. In contrast, the negative photocurrent at the drain was almost unchanged, as shown in Figure 2a(i,ii). Furthermore, the same device with a reversed gate voltage applied but the same amplitude (-2 V) showed the opposite photocurrent behavior: that is, the positive photocurrent at the source greatly enhanced while the negative photocurrent at the drain was improved slightly, as shown in Figure 2c(i,ii). Figure 2a–c(iii) shows the corresponding *I*-*V* characteristics of the same device in the dark and under global illumination. Initially, the device showed a net-output I_{sc} of -0.17 nA and a V_{oc} of 0.03 mV under 405-nm laser irradiation (green line of Figure 2b(iii)). Similarly, by applying a positive gate voltage of 2 V, the device immediately exhibited enhanced *I*-*V* behaviors with an I_{sc} of -3.17 nA and a V_{oc} of 1.38 mV (blue line of Figure 2a(iii)). On the contrary, the same device with an I_{sc} of -0.17 nA and a V_{oc} of 0.03 mV could be immediately regulated to an opposite *I*-*V* behavior with an I_{sc} of 3.3 nA and a V_{oc} of -0.08 mV by applying a gate voltage of -2 V (red line of Figure 2c(iii)). Similar gate-tunable *I*-*V* characteristics were observed at another wavelength (from UV-vis to near IR) under dark and light-illuminating conditions (Figure S7, Supporting Information).

In order to explain the mechanism of the gate-tunable PTE effect in the heterojunction devices, the operation states of the device under different gate voltages are illustrated in Figure 2d–f. In the initial state, as shown in Figure 2e, the electric field in space-charge region will induce the electron state transition from localized state to delocalized state at the interfacial VO₂ layer to maintain the dynamic balance of space charges existed in the n-VO₂/p-GaN heterojunction, and the photocurrent generated at both sides of the drain and the source is almost equal with a net-output I_{sc} of -0.17 nA (Figure 2b). Then, by applying a positive gate voltage of 2 V, as displayed in Figure 2d, the space-charge region will be narrowed to make the interfacial VO₂ near the source side transition back to the localized state, resulting in a significantly reduced positive photocurrent in the source side. In contrast, the drain side remains almost unchanged, so the net-output I_{sc} is -3.17 nA at this state (Figure 2a). Nevertheless, with the applied gate voltage of -2 V, as depicted in Figure 2f, the depletion region will be widened to make more VO₂ near the source side transform into the delocalized state, ultimately resulting in an enhanced positive photocurrent in the source side while the drain side is only changed a little; thus the net-output I_{sc} of 3.3 nA is shown in Figure 2c. Additionally, to demonstrate the non-uniform regulation of gate voltage on the space charge region between the source and the drain terminals, we simulated the potential distributions in the VO₂/GaN heterostructure devices with the COMSOL Multiphysics software (Methods). The results indicate that the space charge region can be significantly regulated near the source. At the same time, the effect is weak near the drain (Figure S7, Supporting Information). More

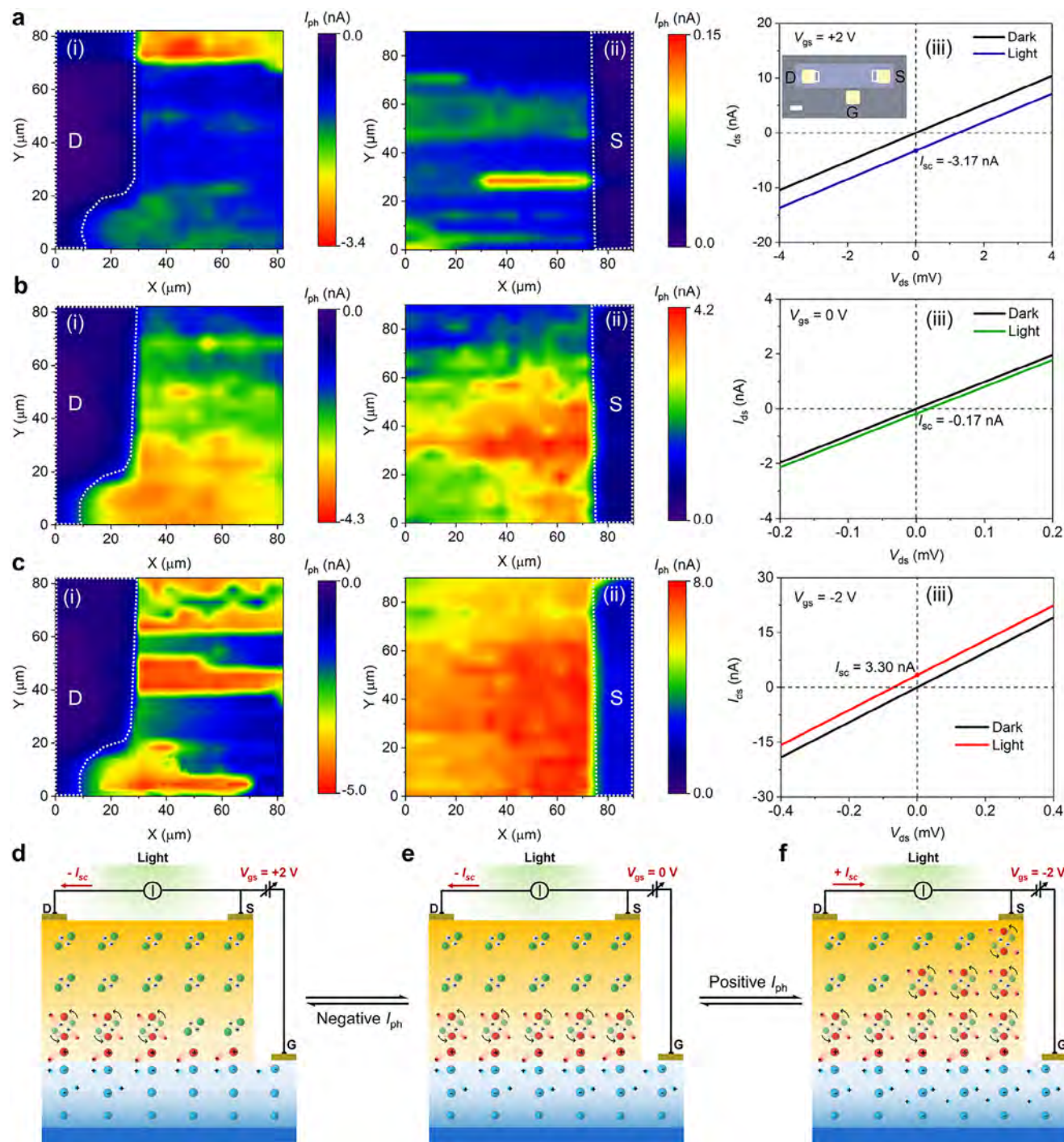


Figure 2. Photocurrent mapping characterization and schematic diagram of VO₂ PTE device under different gating states. a–c) Photocurrent mapping of the drain (i) and source (ii) region of the three-terminal VO₂ heterostructure detector at gate voltages of +2 V (a), 0 V (b), and –2 V (c), respectively. Corresponding I – V characteristics with and without laser irradiation are shown behind them, representing the net output short-circuit current (I_{sc}) generated by PTE effects of the VO₂ channel near the source and the drain (iii). The white-rectangular selections of the inset show the actual mapping areas on the device: scale bar, 100 μm . The photocurrent mapping is all performed under short-circuit conditions with irradiation ($\lambda = 405\text{ nm}$, 0.5 $\text{nW}\ \mu\text{m}^{-2}$ laser power). It is worth noting that the same device was used in the test but that the photocurrent scale of each map remains at an absolute intensity to accommodate the change in channel resistance caused by the phase transition of VO₂. (d–f) Schematic diagram of the tunable VO₂ PTE detector operating at negative and positive states when the gating voltages (V_{gs}) varied from 0 V (e) to +2 V (d) and –2 V (f), respectively.

simulation and mechanistic analyses for the positive and negative photocurrent maps were attached to Notes S2 and S3 (Supporting Information).

2.3. The Coupling Principle of PTE and Phase Transition

As a strongly correlated transition metal oxide, there is a strong coupling relationship between the crystal phase of VO₂ and its electronic state. To understand the microscopic mechanism behind the gate-tunable and broadband responsivity of VO₂ PTE devices, we performed systematic experiments and thorough theoretical calculations. We observed the in situ distribution of crystal phases in the VO₂ channel by applying different gating voltages, creating an out-of-plane electric field of $\approx 10^4$ V cm⁻¹. The red signal in the Raman map shows the distribution of the monoclinic VO₂ phase in the insulated state, and the blue signal represents the distribution of rutile VO₂ in the metallic state in Figure 3a–c. The Raman map and corresponding phase-section profile demonstrate uniform phase distribution of the initial state along the VO₂ channel before gate voltage is applied, as shown in Figure 3b(i,ii). However, using a positive voltage of 2 V on the gate electrode (with source grounded, Figure 3a(i)), the VO₂ channel showed the apparent absence of pristine insulating VO₂ phase near the source side, indicating the transition of VO₂ phase from initial semiconducting state to pristine insulating state, consistent with the phase section profile in Figure 3a(ii).

To demonstrate the opposite phase transition in VO₂ PTE devices, a constant negative (–2 V) voltage was applied to the gate electrode; the VO₂ channel near the source transformed into the metallic phase distribution, indicating the opposite phase-change direction from the initial semiconducting state to semi-metallic state (Figure 3c(i)). The uniform distribution of the metallic VO₂ phase was also observed in the phase section profile, as shown in Figure 3c(ii). The device schematics illustrate the gate-tunable phase transition of the VO₂ layer near the source and drain regions (Figure 3a–c(iii)). Combined with in situ absorption spectrum characteristics (Figure S9a, Supporting Information), we further reveal the phase-change states of VO₂ near the source region. In the initial state, all VO₂ film in the channel was semiconducting induced by the intrinsic space-charge region, consistent with a band gap of 0.46 eV as determined from the Tauc plot (Figure S9b, Supporting Information). However, when applying the positive gate voltage of 2 V, the VO₂ near the source recovered from the semiconductor to the pristine insulating state regulated by the space-charge region, and the band gap was also retrieved from 0.46 to 0.68 eV. In contrast, the space-charge region was broadened by the negative gate voltage of –2 V, which caused the VO₂ near the source to transform into a semi-metallic state, and the corresponding band gap was reduced to 0.27 eV. The changes in Fermi energy (E_F) levels and energy band arrangements are illustrated in Figure S9c (Supporting Information).

Furthermore, first-principles simulations using density function theory (DFT) were also performed to unravel the microscopic mechanism. First, the work function of VO₂ and GaN were calculated, as shown in Figure 3d. According to the experimental results, the VO₂(010) surface and GaN(001) surface were constructed (Figure S10, Supporting Information). The calculated work function values of the VO₂(010) surface and GaN(001) sur-

face were 5.89 and 6.43 eV, respectively. Hence, the electrons flow to GaN from VO₂ when GaN contacts VO₂. Computed differential charge distribution at the GaN/VO₂ interface also shows that VO₂ donates electrons to GaN (Figure 3e), consisting of the calculated work function values. Then, the effect of charge transfer in the heterostructure on the bandgap of VO₂ was examined in Figure S11 (Supporting Information). For the pristine M-VO₂, the calculated bandgap is 0.68 eV, consistent with previous work.^[62] When VO₂ is doped with holes, the bandgap changes, as shown in Figure 3f. Specifically, during the increasing hole density, the bandgaps of VO₂ decrease gradually and become 0 eV. The bandgap of VO₂ in the heterojunction is smaller than pristine VO₂ since holes of GaN flow to VO₂. When a voltage is applied to the heterostructure, the charge transfer between VO₂ and GaN changes, causing a further bandgap shift of VO₂. If the direction of applied voltage is the same as the built-in electric field, more holes will be injected into VO₂; this way, the bandgap of VO₂ decreases further. While the direction of the applied voltage is opposite to the built-in electric field, fewer holes flow to VO₂, and the bandgap of VO₂ increases. The results of the DFT calculations are in agreement with the experimental results. Overall, our results demonstrated that the gate-tunable PTE responsivity of VO₂/GaN heterostructure photodetectors was due to the gate voltage-driven changes of space-charge regions, which dynamically regulated the phase distribution and PTE coupling in the VO₂ channel.

2.4. Gate-Dependent Broadband Photoresponse from Device to Array

Achieving ISIP in PTE heterostructure sensors requires a gate dependence and linear light intensity dependence for the broadband photocurrent. We measured the relationship between the light intensity and broadband photoresponse, as well as the gate voltage at different wavelengths. Figure S12a (Supporting Information) presents the gate-dependent negative and positive photoresponse under a fixed light intensity at a wavelength of 365 nm, and Figure S12b (Supporting Information) demonstrates the negative and positive photoresponses under different light intensities at a wavelength of 365 nm (indicated by shadow zones). It is essential to have a linear intensity dependence on the photocurrent to represent the pixels in broadband images using the light intensity. We replot the power-dependent short-circuit photocurrent and fit these curves with the formula of $I_{sc} \propto P^\alpha$ at different wavelengths (Figures S12c–e and S13b,d, Supporting Information). The fitted results indicate that the extracted values for α are almost equal to 1 for all the wavelengths used in the experiment. The excellent linear mapping between the photocurrent and laser intensity ensures sensing precision. Similarly, we replot the experimental data for the gate-tunable negative and positive photoresponse for different wavelengths (Figures S12f–h and S13a,c, Supporting Information) and fit these data to linear equations. Under the same gate voltage and light intensity, the photoresponse for irradiation at 365, 532, and 808 nm is tunable from –110 to 240 $\mu\text{A W}^{-1}$, from –120 to 220 $\mu\text{A W}^{-1}$, and from –115 to 210 $\mu\text{A W}^{-1}$, respectively. The fitting results show that the photocurrent can be linearly regulated by the applied gate voltage for the given light intensities and wavelengths. It is worth noting

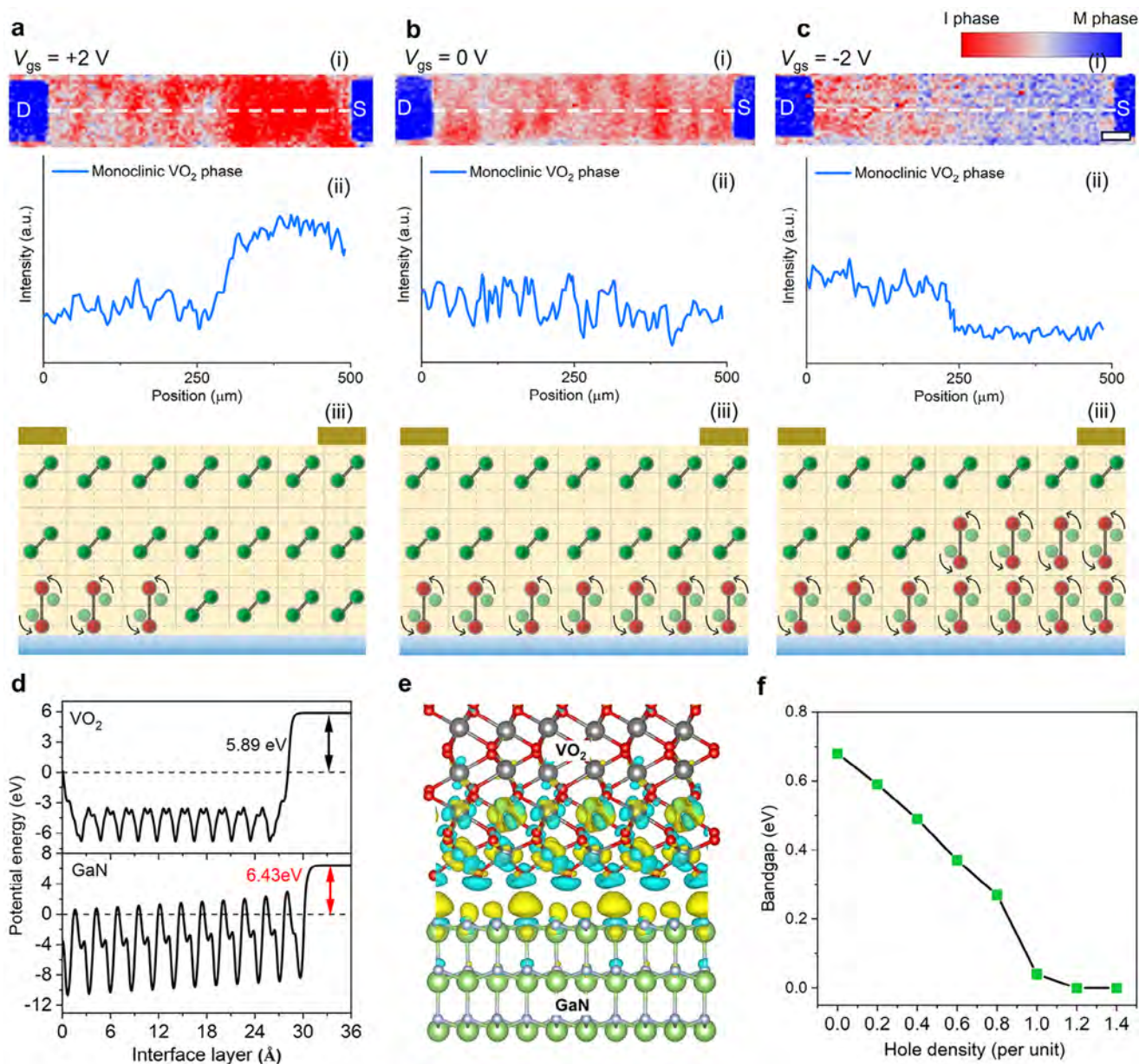


Figure 3. In situ Raman mapping of the gate-tunable VO_2 PTE devices and DFT simulation. a–c) The Raman mapping images (i) for phase distribution along the drain and source regions, corresponding mapping section profile (ii), and schematic diagram (iii) of the tunable VO_2 PTE device working at different states when the gate voltage is +2 V (a), 0 V (b) and –2 V (c), respectively. Raman map shows varied phase distribution in the VO_2 channel regulated by positive or negative gating voltages with $V_{ds} = 0\text{ V}$. Scale bar, 50 μm . Green sphere, monoclinic vanadium; red sphere, rutile vanadium; golden and blue rectangle, metal. d) Computed potential energy with workfunction value for VO_2 (010) and GaN(001). The Fermi level is set to zero. e) Computed differential charge distribution at VO_2 (010)/GaN(001) interfaces. Blue and yellow bubbles represent hole and electron charges, respectively. Gray, red, green, and silvery beads represent V, O, Ga, and N atoms, respectively. f) Bandgaps of monoclinic VO_2 doped with hole.

that a linear window can be maintained for a voltage of $\approx 6\text{ V}$. This characteristic enables simple and fast tuning of convolution kernels of ISIP.

In addition, broadband gate-tunable VO_2 PTE devices exhibit the potential for large-scale array fabrication compatible with standard CMOS foundry processes. As a demonstration, we fabricated, in-house, 900 of the gate-tunable VO_2 PTE detectors on a two-inch commercial GaN wafer (Figure 4a, left) using CMOS-compatible fabrication (Methods). The fabricated wafer features

$3 \times 3 = 9$ reticles, each containing $10 \times 10 = 100$ PTE detectors (Figure 4a, right). We randomly selected 200 devices from the arrays and examined their channel resistance and gate-tunable photoresponsibility (Figure 4b–d). As shown in Figure 4b, the I – V curves distribution of the devices is relatively narrow, and the resistance histogram (Figure 4b inset) shows that the overall device resistance of VO_2 on the GaN wafer is $\approx 60\text{ k}\Omega$, which reflects the uniformity of the film growth. Figure 4c shows the photocurrent maps obtained by irradiating a 405 nm laser with a fixed

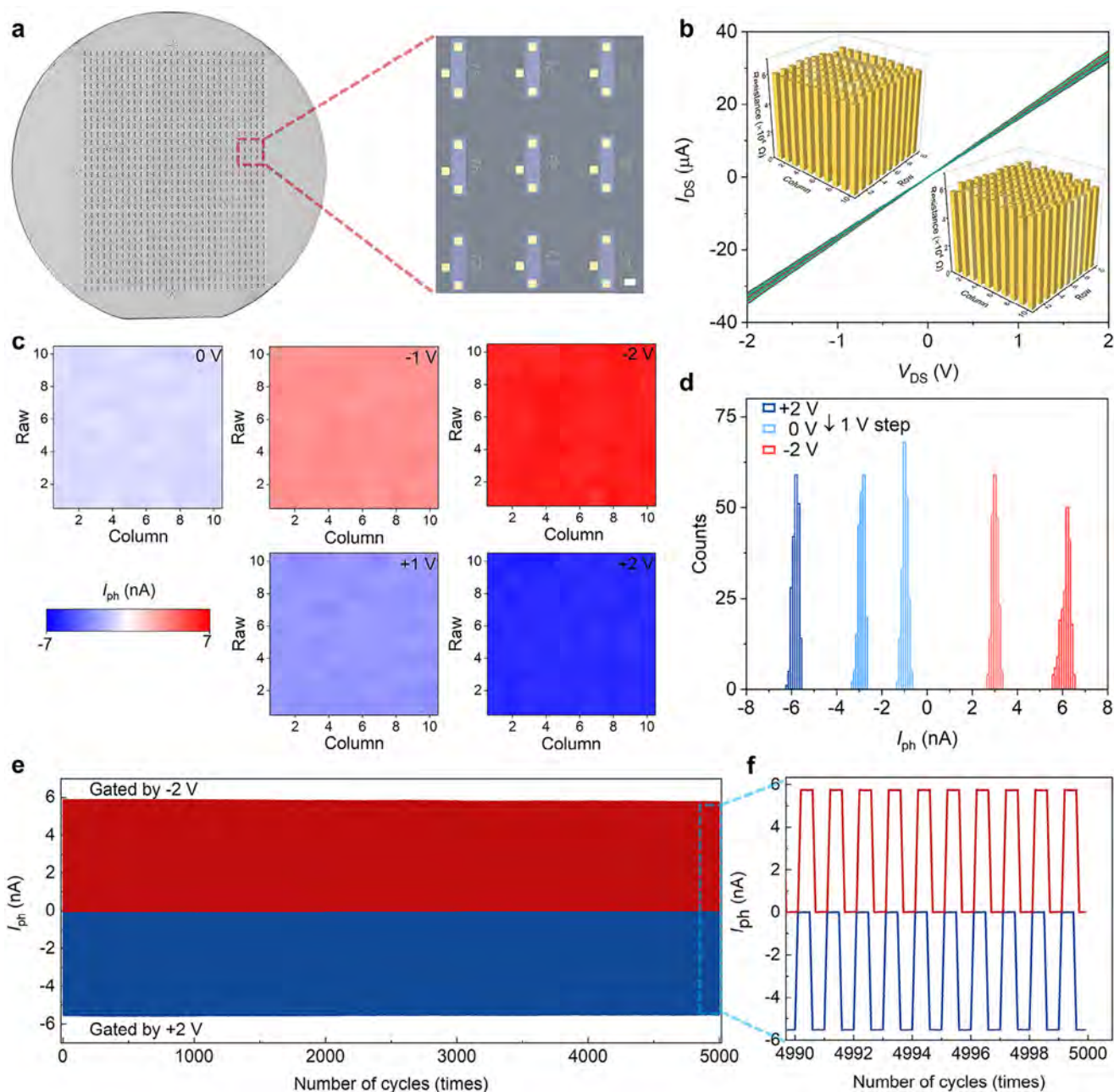


Figure 4. Wafer-scale arrays of the gate-tunable VO₂ PTE devices. a) Optical images of a fabricated two-inch wafer containing 30 × 30 PTE devices (left) and a magnified image of nine examples of the PTE devices (right). b) *I*–*V* curves of 200 devices selected from the arrays. Inset: Statistics histogram of the channel resistance for these extracted devices. c) Photocurrent map of a random reticle (10 × 10 PTE detectors) with gate voltage varied from –2 to 2 V with a 1 V step. d) Histogram of the photocurrent data collected in (c), with gate voltage from –2 V (blue) to 2 V (red) shown in 1 V increments for clarity. e) Time-resolved positive and negative photoresponses of the VO₂ PTE detector for 5000 cycles operation at a gate voltage of –2 V and +2 V, respectively. f) Local enlarged image of (e) for the last ten light responses. All the measurements in this figure were performed with a 405 nm laser source at a power density of 0.73 nW μm^{–2}.

power density of 0.73 nW μm^{–2} serially, device by device, across an example reticle containing 100 PTE detectors, for varied gate voltage from –2 to 2 V with a 1 V step. These maps show that the responsivity programming within the reticle is highly uniform from device to device. Figure 4d shows the distribution of the 100 photocurrents for selected gate voltage values (–2 to 2 V with a 1 V step), where the variations from device to device are more

pronounced than those of the single reticle, which is standard at the wafer scale. Concretely, as we sweep the gate voltage, the photocurrents of the 100 devices, in response to the 405 nm laser irradiation with a fixed power density of 0.73 nW μm^{–2}, varied from -5.8 ± 0.3 to 6.2 ± 0.5 nA, although there is relatively low energy-conversion efficiency with the *I*_{sc} of –5.5 or 5.7 nA with applying a gate of 2 or –2 V, respectively, the weak PTE behavior can enable

the present device to function as a self-powered photodetector, producing obvious photoresponse (Figure 4e). Further photoresponse analysis in Figure 4f reveals that the VO₂ PTE detector can be easily switched between on and off states with perfect reproducibility and stability by repeatedly turning light (405 nm) on and off, even after 5000 cycles of operation at positive or negative gate voltage state. Unlike other dual-mode devices induced by ionic migration or ferroelectric polarization subject to inherent limitations, such as defect accumulation and structural collapse, the VO₂-based detector shows more constant bipolar photocurrent signals due to the distinct Mott phase transition characteristics, which do not cause structural damage.

2.5. Implementations of ISIP

By modulating the bias voltages of the gate of VO₂ PTE devices (PTEDs), we demonstrate broadband ISIP. As a proof of concept, we used a single device to receive each pixel image one by one and perform the ISIP. We first validate this by extracting spectral and spatial features in remote sensing images from Urban hyperspectral datasets,^[63] encompassing components, such as *Asphalt*, *Grass*, *Trees*, and *Roofs* (Figure 5a). Here, we employ three popular image-processing convolutional kernels: original, sharpness, and edge enhancement. They are simulated by 3 × 3 VO₂ PTED arrays with gate voltages shown in Figure 5b. For the original kernel, as the gate voltages are zero, no discernible information content is observed in the input of the UV band, Vis band, and NIR band, leaving only the original information displayed (Figure 5b). For the sharpness kernel, a voltage of 3 V is applied around the perimeter and -3 V in the center, which enhances image clarity across different wavelengths of UV, Vis, and NIR (Figure 5c). For the edge enhancement kernel, the gate voltage patterns make the summed PTED output currents, enhancing the difference between adjacent pixels and enhancing edges (Figure 5d). The performance of different wavelength inputs under different voltages can be seen in Figure S14 (Supporting Information). In addition, we also conducted a generalization ability validation on the Jasper Ridge dataset, which can be found in Figure S15, Supporting Information.

Beyond simple feature extraction, we use broadband PTED convolutional kernels with a deep neural network (DNN) for hyperspectral image classification. Our classification framework comprises two main operations: convolution and fully connected layers. The convolution utilizes PTE kernels to extract features of the University of Trento (UT) dataset^[64] across the UV, VIS, and NIR wavelength channels. Once extracted by the PTE, these features are processed through the fully connected layers executed on a computer. The PTED-based neural network shows classification accuracy close to that of the software. Specifically, Figure 5f displays the 2D distribution of in-sensor broadband DNN features following t-Distributed Stochastic Neighbor Embedding (t-SNE) dimensionality reduction, unveiling a distinct separation between various categories, including *Woods*, *Apples*, *Vineyards*, *Buildings*, *Roads*, and *Ground*. Figure 5g showcases the confusion matrix of different categories on the test dataset, dominated by diagonal elements, indicative of high accuracy. The t-SNE and confusion matrix without the PTEDs array can be found in Figure S16, Supporting Information. Figure 5h presents the accuracy

of each category and the overall accuracy. Compared to software-based methods, our system exhibits similar accuracy in both individual categories and overall accuracy. The training process for software-based models and those with the PTEDs array can be found in Figure S17, Supporting Information.

In addition to image classification, we validate our system on image denoising, a representative reconstruction task.^[65,66] Figure 6a underscores the significant potential of in-sensor neuromorphic denoising within the medical imaging domain by utilizing an in-sensor VO₂ PTED array. Our approach involves a model structure comprising the in-sensor PTED array, simulated to implement the first convolutional layer of a UNet. The input consists of noisy medical images from the Med-MNIST dataset.^[76] At the same time, the output is denoised images for better medical diagnosis (Figure 6a). For the denoising task, noisy input images (Figure 6b) are converted to the optical illumination pattern to the VO₂ PTED array. The conductance of each device within the array is modulated by the gate voltage to physically implement convolutional kernels. The extracted feature maps, in the form of currents, are subsequently digitized and sent to a digital computer to go through the rest of the encoder and decoder layers (Figure 6c). Ultimately, denoised medical images are displayed from top to bottom as *HeadCT*, *BreastMRI*, and *AbdomenCT* images. Our analysis reveals that the denoising effect of the VO₂ sensor is consistent with the state-of-the-art software (Figure 6d).

Furthermore, we demonstrate the medical segmentation for bio-retinal blood vessels using the Digital Retinal Images for Vessel Extraction (DRIVE) dataset,^[67] which comprises 40 color fundus images, including seven abnormal pathology cases. The visible light optical image (Figure 6e) is received by the VO₂ PTED array, which simulates the implementation of the first convolutional layer of the UNet, similar to the denoising case. The digitized PTED array outputs pass through the rest of the UNet and produce segmented output. The VO₂-based segmentation (Figure 6e) aligns closely with the software and Ground Truth. Figure 6f presents the VO₂-based receiver operating characteristic (ROC) results, achieving a performance of up to 0.9799 based on the VO₂ PTED array, comparable to the 0.9791 of the state-of-the-art software baselines. Additionally, the confusion matrix reveals a robust, dense classification performance of 98.10% for the VO₂ PTE-based array and 98.28% for the software-based model, consistent with state-of-the-art results. The PTED exhibits lower energy consumption compared to a digital computer performing denoising (segmentation) tasks, in which the experimental/optimal energy consumption can be reduced by $\approx 315.49/\approx 63098.59$ times and $\approx 709.85/\approx 141971.83$ times, respectively. A detailed comparison of energy consumption between the PTEDs array and software processes, specifically for denoising and segmentation tasks, is provided in Figure S18, Supporting Information.

3. Conclusion

In summary, we have reported reconfigurable and broadband PTE detector devices based on a simple planar JFET architecture with VO₂/Ga_{0.5}N heterojunctions. The regulation of phase distribution near the source caused by gating voltage in the devices results in a gate-tunable, polar-variable PTE response, which can

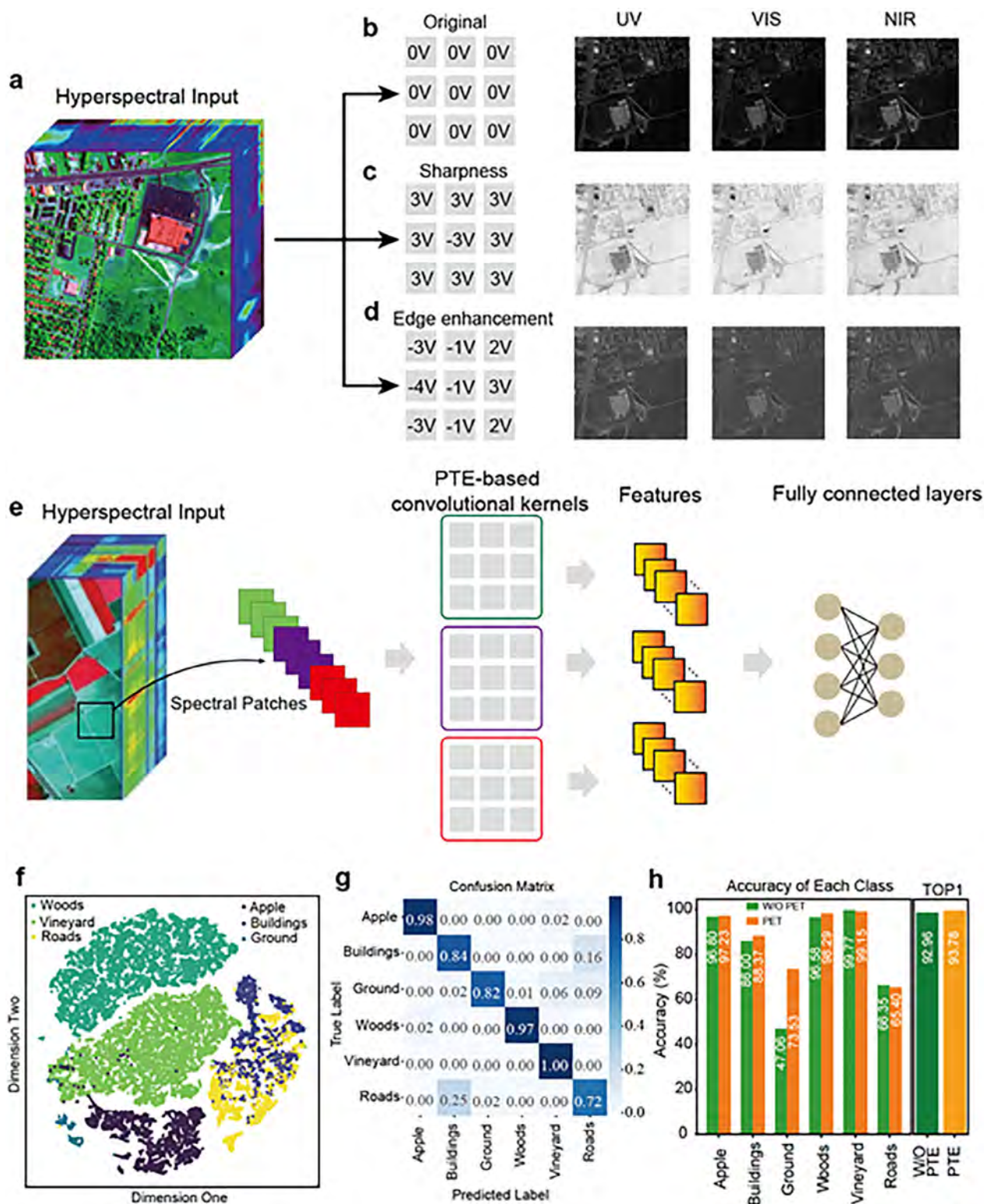


Figure 5. PTE devices for in-sensor imaging processes. a) Demonstrating various image processing operations, including sharpness and edge enhancement, using UV, Vis, and NIR wavelengths. b) Original image. c) Images showcasing sharpness. d) Images highlighting edge enhancement. e) PTE-based deep learning models featuring convolutional and fully connected layers for hyperspectral image classification. f) The t-SNE distribution of PTE-based DLs. g) Confusion matrix for classifying the University of Trento (UT) test dataset. h) A comparison of each class accuracy and Top1 accuracy between the PTE-based hardware system and the pure digital computer system, where Top1 accuracy refers to the percentage of times the model's top prediction matches the true label.

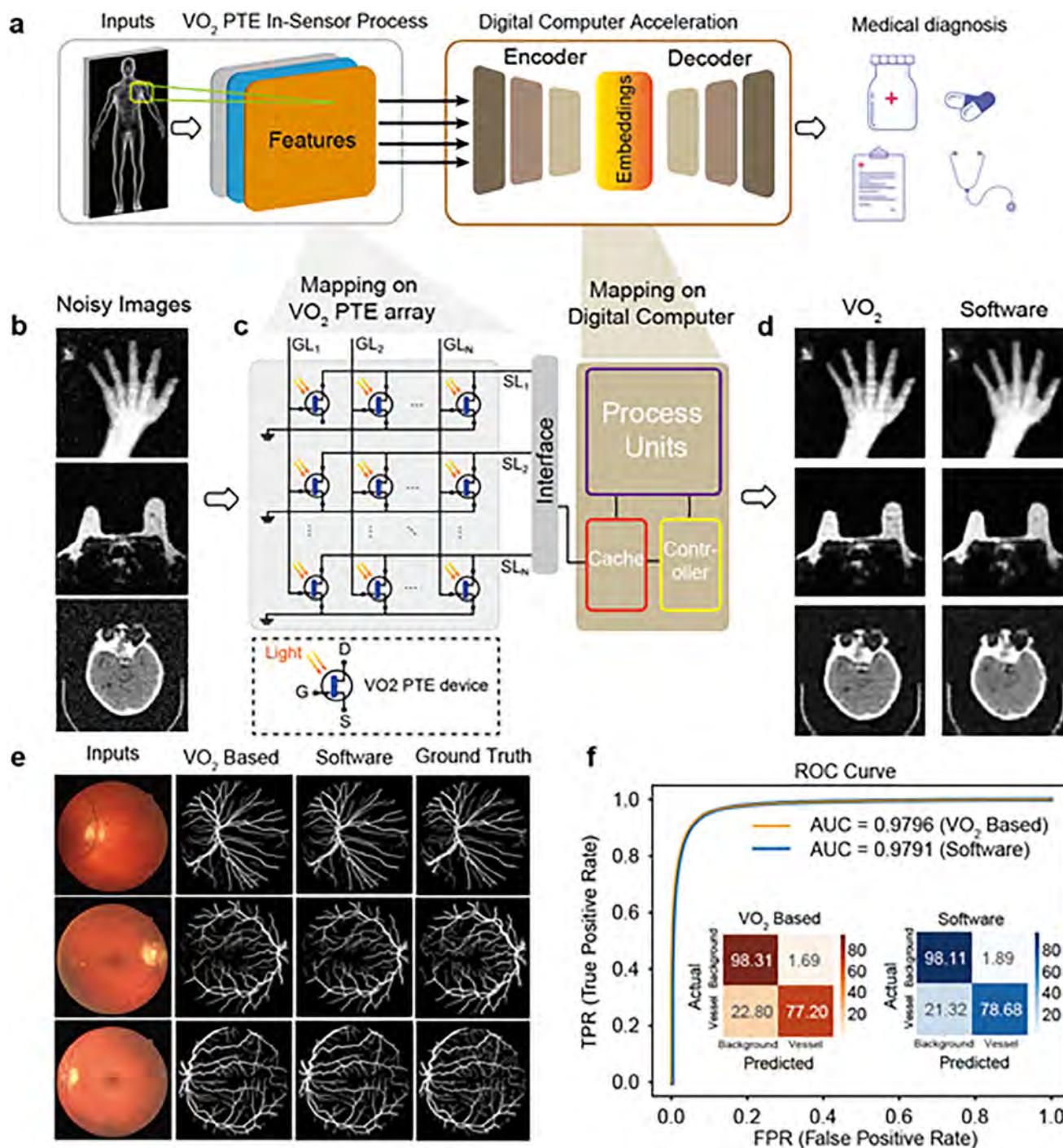


Figure 6. Denoising and semantic segmentation on PTE-based in-sensor arrays. a) The VO_2 PTE in-sensor array-based autoencoder system for human medical diagnosis. b) Noisy CT images affected by environmental factors. c) VO_2 PTEs arrays for preprocessing the noisy input images, with autoencoder parameters mapped on digital computers. d) Denoised images produced by the VO_2 PTE-based and software convolution kernels-based denoising system. e) Retinal images comparing vessel extraction between the VO_2 -based UNet, software convolutional-based UNet, and the ground truth. f) ROC curve and confusion matrix of VO_2 -based UNet and software-based convolutional-based UNet for pixel-wise blood vessel classification, characterized by prominent diagonal elements, where the ROC curve is plotted by calculating the True Positive Rate (TPR) and False Positive Rate (FPR) at different classification thresholds to evaluate the performance of a binary classifier.

be used to build optical in-sensor hardware for simultaneous broadband sensing and convolutional processing. The energy consumption for a single event of this device is one order of magnitude lower than that of comparable VO₂-based ISIP devices. Furthermore, we fabricated a wafer-scale integrated PTE sensor array and proved that the VO₂ film on the commercial wafer also achieves stable and repeatable PTE imaging capabilities. The linear relationship between broadband photocurrent, light intensity, and gate voltage allows for a convolutional network utilizing the VO₂ heterostructure sensor in broadband image classification, medical image denoising, and vessel extraction for retinal images. Compared to software processes, our PTED can save hundreds times of energy consumption. These applications lay the groundwork for implementing future ISIP with Mott-transition-based PTE activation.

4. Experimental Section

Device Fabrication: First, the commercial p-type GaN (Mg-doped, hole concentration $\approx 1.4 \times 10^{17} \text{ cm}^{-3}$) on c-plane sapphire grown by MOCVD was chosen as the epitaxial substrate. The monoclinic VO₂ films were deposited on this p-GaN (0001) layer by an RF-plasma-enhanced reactive magnetron sputtering under a power of 100 W with argon-oxygen flow ratio of 10:1 at a pressure of 3 mTorr. The growth thickness and rate were monitored by a crystal oscillator (SQC-310, INFICON). Then, the VO₂ pattern arrays were fabricated by the standard wet-etching process with a phosphoric acid solution. After that, the position of electrode patterns was defined by UV lithography and then exposed to the phosphoric acid etching solution, while the VO₂ channel was protected by a photolithography-patterned photoresist. Finally, the 5 nm Ti and 50 nm Au layers were deposited on VO₂ by electron beam and thermal evaporations with a base pressure of 2×10^{-6} Torr and a deposition rate of 1 \AA s^{-1} , followed by the standard lift-off process.

STEM Imaging and EDS Mapping: High-resolution transmission electron microscopy (JEOL JEM-ARM300F2) analysis was conducted to obtain the cross-sectional image of the device with an operation voltage of 300 kV. HAADF-STEM was performed on a spherical-aberration-corrected mode to observe the clear atomic image of the samples. The sample was sliced by a focused ion beam (FEI, Helios NanoLab650) with a C passivation layer for the TEM analysis. The distribution of elements was obtained from the EDS mapping in the materials.

Raman and Absorption Measurements: In-situ Raman spectra were performed by the WITec Alpha 300R Raman system. The excitation wavelength was 532 nm, and the laser power was 2 mW. Raman imaging measurements were carried out using the ultrafast mapping mode with an integrated intensity range from 166 to 246 cm^{-1} . All spectral data were imaged using the pinch-peak method after deducting the back base using WITec Project 5 software. In situ absorption spectra were collected using a Hitachi UH4150 UV-Vis-NIR spectrophotometer equipped with a commercial microprobe station (MPS-PTH, NEXTRON). All gate voltages for in situ tests were supported by a Keysight B2912A source meter. All the measurements were carried out in an ambient environment at room temperature.

XRD and XPS Measurements: The crystal structure of all samples was characterized by an X-ray Diffractometer (SmartLab 9 kW, Rigaku) with Cu K α radiation ($\lambda = 1.54178 \text{ \AA}$). The VO₂/GaN heterostructure device morphology was characterized by optical microscopy (BX53 M, Olympus). XPS (ESCLAB Xi+, Thermo Fisher) characterizations were performed using an Al K α X-ray with photon energies of 1486.6 eV working under a base vacuum lower than 10^{-10} Torr. The source was operated at 15 kV with an emission current of 4.5 mA.

Device Characterization: The electrical measurements of the devices were conducted using a commercial semiconductor analyzer (B1500A, Keysight) in a Lake Shore probe station. The lasers used in this work were

guided by an optical fiber focused on the device with a microscope system and calibrated by a power meter (PM400, Thorlabs). A homemade light chopper and an attenuator were used to control the laser on/off and its intensity. The response time data were acquired using an oscilloscope (MDO3014, Tektronix). An optoelectronic testing system (ScanPro Advance, METATEST) was employed to obtain photocurrent mapping data, using a 405 nm multimode laser as the light source.

COMSOL Simulations: Simulations using the finite-element method (FEM) were performed with Comsol 5.4 (COMSOL, Inc.) using the built-in AC/DC model. Where needed, the cell geometries were rebuilt in 3D from the design values and optical images. The room-temperature conductivity and relative dielectric constants of the VO₂ and GaN thin-film layer were $\approx 1.0 \text{ S cm}^{-1}$, $\approx 0.07 \text{ S cm}^{-1}$, ≈ 36 , and ≈ 8.9 , respectively, combined with the previous reports.^[68–71] More details of the FEM simulations are provided in Figure S8 and Note S2 (Supporting Information).

First-Principles Calculations: All calculations were performed with density functional theory (DFT) using the Vienna ab initio simulation package (VASP) code.^[72] The exchange and correlation terms were described using general gradient approximation (GGA) in the scheme of Perdew–Burke–Ernzerhof (PBE).^[73] Core electrons were described by pseudopotentials generated from the projector augmented-wave method.^[74] and valence electrons were expanded in a plane-wave basis set with an energy cutoff of 450 eV. The VO₂(010) surface, GaN(001) surface and VO₂(010)/GaN(001) interface were modeled by slab method. VO₂(010)/GaN(001) interface was constructed by (1×1) VO₂(010) and $(\sqrt{3} \times \sqrt{3})$ GaN(001). The thickness values of the vacuum in the surface and interface model were set to be larger than 15 Å. The DFT+U method was employed for VO₂, and the value of U was used as 3.4 eV. The geometry relaxation was carried out until all forces on the free ions were converged to 0.01 eV \AA^{-1} .

Datasets Used for Experimental Measurements: Figure 5a's urban dataset, widely used in hyperspectral unmixing studies, contains 307×307 pixels (each $2 \times 2 \text{ m}^2$) and 210 wavelengths (400–2500 nm) with a 10 nm resolution. 405 nm UV, 532 nm Vis, and 808 nm NIR channel images were extracted for experimentation. The UT dataset in Figure 5e, collected with an AISA Eagle sensor in southern Trento, Italy, had 600×166 pixels and 63 spectral bands (0.42–0.99 μm), featuring six exclusive vegetation land-cover classes, a 9.2 nm spectral resolution, and a 1 MPP spatial resolution. 405 nm UV, 532 nm Vis, and 808 nm NIR channel images were used for convolution operations. Figure 6b's MedMNIST dataset (<https://www.kaggle.com/datasets/andrewmvd/medical-mnist>) includes 58954 MNIST-style 64×64 medical images across six classes: AbdomenCT, BreastMRI, CXR, ChestCT, Hand, and HeadCT. HeadCT, BreastMRI, and AbdomenCT images were selected for denoising experiments. The DRIVE dataset in Figure 6e, designed for retinal vessel segmentation, comprises 40 JPEG color fundus images, including seven abnormal pathology cases. Obtained through a diabetic retinopathy screening program in the Netherlands, images were captured using a Canon CR5 non-mydiatric 3CCD camera with a 45-degree FOV. Each image had a 584×565 resolution with eight bits per color channel (3 channels) and was equally divided into training and testing sets (20 images each). For MedMNIST and DRIVE datasets using visible light range input images, PTE in-sensor processing was applied at 450, 532, and 635 nm across the three channels.

Simulation Details: In Figure 5e's classification task on the UT dataset, the PTE array-based model comprises two downsampling Conv2d layers and one fully connected layer, with the PTE method implementing the first Conv2d layer. For the MedMNIST denoising task in Figure 6b, the employed UNet consists of two downsampling Conv2d layers and two upsampling ConvTranspose2d layers. In Figure 6e's image segmentation task, the UNet utilizes the state-of-the-art LADDERNET.^[75] In these processes, the first layer for both tasks was implemented by PTE, while the comparison tasks employ software-based Conv2d. All simulations were conducted using Python and PyTorch and executed on a GPU.

Supporting Information

Supporting Information is available from the Wiley Online Library or from the author.

Acknowledgements

This research was financially supported by the Research Grants Council of the Hong Kong Special Administrative Region, China (Project No. CRS_CityU101/24), the Innovation and Technology Fund (MHP/044/23) from the Innovation and Technology Commission of the Hong Kong Special Administrative Region, China, the Science Technology and Innovation Committee of Shenzhen Municipality (Project No. JCYJ20230807114910021), and Guangdong Basic and Applied Basic Research Fund (Project no. 2024A1515011922).

Conflict of Interest

The authors declare no conflict of interest.

Author Contributions

B.L., N.L., and Z.W. contributed equally to this work. B.W.L. and J.C.H. conceived and initiated the project. B.W.L. prepared materials and fabricated devices and performed all characterization analyses. N.L. and Z.R.W. performed the ISIP simulations and results analysis. Z.W.W. performed the DFT calculation. B.J.C. and C.H.C. performed integrated fabrication and test. C.Y.L. and Y.M. performed the photocurrent mapping and analysis. M.Q.D. performed the FE simulations. X.C.L. and F.R.C. performed the AC-TEM measurement and analysis. W.J.W. and Z.H.W. performed part of the analysis. Y.M., P.S.X., Y.X.Z., and D.J.L. helped with electrical measurement and analysis. B.W.L., N.L., Z.W.W., Z.R.W., and J.C.H. analyzed the data and wrote the initial manuscript. All authors contributed to the final manuscript and approved the submission.

Data Availability Statement

The data that support the findings of this study are available from the corresponding author upon reasonable request.

Keywords

bipolar photoresponsivity, in-sensor processing, phase transition, photothermoelectric detector

Received: February 12, 2025

Revised: April 10, 2025

Published online:

- [1] L. Portilla, K. Loganathan, H. Faber, A. Eid, J. G. D. Hester, M. M. Tentzeris, M. Fattori, E. Cantatore, C. Jiang, A. Nathan, G. Fiori, T. Ibn-Mohammed, T. D. Anthopoulos, V. Pecunia, *Nat. Electron* **2023**, 6, 10.
- [2] R. Napolitano, W. Reinhart, J. P. Gevaudan, *Science* **2021**, 371, 1200.
- [3] J. L. Pan, J. McElhannon, *IEEE Internet Things* **2018**, 5, 439.
- [4] M. El Jarroudi, L. Kouadio, P. Delfosse, C. H. Bock, A.-K. Mahlein, X. Fettweis, B. Mercatoris, F. Adams, J. M. Lenné, S. Hamdioui, *Nat. Sustain.* **2024**, 7, 846.
- [5] Z. Yang, T. Wang, Y. Lin, Y. Chen, H. Zeng, J. Pei, J. Wang, X. Liu, Y. Zhou, J. Zhang, X. Wang, X. Lv, R. Zhao, L. Shi, *Nature* **2024**, 629, 1027.
- [6] *Nature, E., Nature* **2018**, 554, 145.
- [7] I. L. Markov, *Nature* **2014**, 512, 147.
- [8] Y. Zhang, P. Qu, Y. Ji, W. Zhang, G. Gao, G. Wang, S. Song, G. Li, W. Chen, W. Zheng, F. Chen, J. Pei, R. Zhao, M. Zhao, L. Shi, *Nature* **2020**, 586, 378.
- [9] Z. Sun, S. Kvatinsky, X. Si, A. Mehonic, Y. M. Cai, R. Huang, *Nat. Electron.* **2023**, 6, 823.
- [10] C. Ma, S. Yuan, P. Cheung, K. Watanabe, T. Taniguchi, F. Zhang, F. Xia, *Nature* **2022**, 604, 266.
- [11] Y. Chai, *Nature* **2020**, 579, 32.
- [12] F. C. Zhou, Y. Chai, *Nat. Electron* **2020**, 3, 664.
- [13] J. A. Leñero-Bardallo, T. Serrano-Gotarredona, B. Linares-Barranco, *IEEE J. Solid-St. Circ.* **2011**, 46, 1443.
- [14] Y. K. Yang, C. Pan, Y. X. Li, X. Yangdong, P. F. Wang, Z. A. Li, S. Wang, W. T. Yu, G. Y. Liu, B. Cheng, Z. F. Di, S. J. Liang, F. Miao, *Nat. Electron.* **2024**, 7, 225.
- [15] Z. Zhang, S. Wang, C. Liu, R. Xie, W. Hu, P. Zhou, *Nat. Nanotechnol.* **2022**, 17, 27.
- [16] L. Mennel, J. Symonowicz, S. Wachter, D. K. Polyushkin, A. J. Molina-Mendoza, T. Mueller, *Nature* **2020**, 579, 62.
- [17] L. J. Pi, P. F. Wang, S. J. Liang, P. Luo, H. Y. Wang, D. Y. Li, Z. X. Li, P. Chen, X. Zhou, F. Miao, T. Y. Zhai, *Nat. Electron.* **2022**, 5, 248.
- [18] T. Li, J. Miao, X. Fu, B. Song, B. Cai, X. Ge, X. Zhou, P. Zhou, X. Wang, D. Jariwala, W. Hu, *Nat. Nanotechnol.* **2023**, 18, 1303.
- [19] G. Wu, X. Zhang, G. Feng, J. Wang, K. Zhou, J. Zeng, D. Dong, F. Zhu, C. Yang, X. Zhao, D. Gong, M. Zhang, B. Tian, C. Duan, Q. Liu, J. Wang, J. Chu, M. Liu, *Nat. Mater.* **2023**, 22, 1499.
- [20] E. Hittinger, P. Jaramillo, *Science* **2019**, 364, 326.
- [21] P. Wu, T. Zhang, J. Zhu, T. Palacios, J. Kong, *Nat. Mater.* **2024**, 23, 23.
- [22] A. Quellmalz, X. J. Wang, S. Sawallich, B. Uzlu, M. Otto, S. Wagner, Z. X. Wang, M. Precht, O. Hartwig, S. W. Luo, G. S. Duesberg, M. C. Lemme, K. B. Gylfason, N. Roxhed, G. Stemme, F. Niklaus, *Nat. Commun.* **2021**, 12, 917.
- [23] D. J. Trainer, J. Nieminen, F. Bobba, B. K. Wang, X. X. Xi, A. Bansil, M. Iavarone, *NPJ 2D Mater. Appl.* **2022**, 6, 13.
- [24] S. Oh, Y. Shi, J. Del Valle, P. Salev, Y. Lu, Z. Huang, Y. Kalcheim, I. K. Schuller, D. Kuzum, *Nat. Nanotechnol.* **2021**, 16, 680.
- [25] G. Li, D. Xie, H. Zhong, Z. Zhang, X. Fu, Q. Zhou, Q. Li, H. Ni, J. Wang, E. J. Guo, M. He, C. Wang, G. Yang, K. Jin, C. Ge, *Nat. Commun.* **2022**, 13, 1729.
- [26] M. Samizadeh Nikoo, R. Soleimanzadeh, A. Krammer, G. Migliato Marega, Y. Park, J. Son, A. Schueler, A. Kis, P. J. W. Moll, E. Matioli, *Nat. Electron.* **2022**, 5, 596.
- [27] Z. Yang, C. Ko, S. Ramanathan, *Annu. Rev. Mater. Res.* **2011**, 41, 337.
- [28] K. Liu, S. Lee, S. Yang, O. Delaire, J. Wu, *Mater. Today* **2018**, 21, 875.
- [29] R. Shi, N. Shen, J. Wang, W. Wang, A. Amini, N. Wang, C. Cheng, *Appl. Phys. Rev.* **2019**, 6, 011312.
- [30] S. Bhupathi, S. C. Wang, Y. J. Ke, Y. Long, *Mat. Sci. Eng. R* **2023**, 155, 100747.
- [31] S. Chen, Z. Wang, H. Ren, Y. Chen, W. Yan, C. Wang, B. Li, J. Jiang, C. Zou, *Sci. Adv.* **2019**, 5, aav6815.
- [32] Z. W. Shao, A. B. Huang, C. C. Cao, X. W. Ji, W. Hu, H. J. Luo, J. Bell, P. Jin, R. G. Yang, X. Cao, *Nat. Sustain.* **2024**, 7, 796.
- [33] K. Tang, K. Dong, J. Li, M. P. Gordon, F. G. Reichertz, H. Kim, Y. Rho, Q. Wang, C. Y. Lin, C. P. Grigoropoulos, A. Javey, J. J. Urban, J. Yao, R. Levinson, J. Wu, *Science* **2021**, 374, 1504.
- [34] B. Wu, Z. Zhang, B. Chen, Z. Zheng, C. You, C. Liu, X. Li, J. Wang, Y. Wang, E. Song, J. Cui, Z. An, G. Huang, Y. Mei, *Sci. Adv.* **2023**, 9, adi7805.
- [35] J. King, C. Wan, T. J. Park, S. Deshpande, Z. Zhang, S. Ramanathan, M. A. Kats, *Nat. Photon.* **2023**, 18, 74.
- [36] J. Ordóñez-Miranda, Y. Ezzahri, J. A. Tiburcio-Moreno, K. Joulain, J. Drevillon, *Phys. Rev. Lett.* **2019**, 123, 025901.
- [37] B. Varghese, R. Tamang, E. S. Tok, S. G. Mhaisalkar, C. H. Sow, *J. Phys. Chem. C* **2010**, 114, 15149.
- [38] T. Yajima, T. Nishimura, A. Toriumi, *Nat. Commun.* **2015**, 6, 10104.
- [39] N. Shukla, A. V. Thathachary, A. Agrawal, H. Paik, A. Aziz, D. G. Schlom, S. K. Gupta, R. Engel-Herbert, S. Datta, *Nat. Commun.* **2015**, 6, 7812.

- [40] Y. J. Lee, K. Hong, K. Na, J. Yang, T. H. Lee, B. Kim, C. W. Bark, J. Y. Kim, S. H. Park, S. Lee, H. W. Jang, *Adv. Mater.* **2022**, *34*, 2203097.
- [41] M. Kumar, S. Lim, J. Kim, H. Seo, *Adv. Mater.* **2023**, *35*, 2210907.
- [42] M. Nakano, K. Shibuya, D. Okuyama, T. Hatano, S. Ono, M. Kawasaki, Y. Iwasa, Y. Tokura, *Nature* **2012**, *487*, 459.
- [43] J. Jeong, N. Aetukuri, T. Graf, T. D. Schladt, M. G. Samant, S. S. P. Parkin, *Science* **2013**, *339*, 1402.
- [44] Z. H. Long, Y. Zhou, Y. C. Ding, X. Qiu, S. Poddar, Z. Y. Fan, *Nat. Rev. Mater.* **2025**, *10*, 128.
- [45] Y. Zhou, S. Ramanathan, *J. Appl. Phys.* **2012**, *112*, 074114.
- [46] Y. Liu, N. O. Weiss, X. D. Duan, H. C. Cheng, Y. Huang, X. F. Duan, *Nat. Rev. Mater.* **2016**, *1*, 16042.
- [47] S. Feng, J. Li, L. Feng, Z. Liu, J. Wang, C. Cui, O. Zhou, L. Deng, H. Xu, B. Leng, X. Q. Chen, X. Jiang, B. Liu, X. Zhang, *Adv. Mater.* **2023**, *35*, 2308090.
- [48] Y. Xu, X. Xu, Y. Huang, Y. Tian, M. Cheng, J. Deng, Y. Xie, Y. Zhang, P. Zhang, X. Wang, Z. Wang, M. Li, L. Li, M. Liu, *Adv. Mater.* **2024**, *36*, 2402903.
- [49] W. Wu, X. Han, J. Li, X. Wang, Y. Zhang, Z. Huo, Q. Chen, X. Sun, Z. Xu, Y. Tan, C. Pan, A. Pan, *Adv. Mater.* **2021**, *33*, 2006006.
- [50] F. Y. Liao, Z. Zhou, B. J. Kim, J. W. Chen, J. L. Wang, T. Q. Wan, Y. Zhou, A. T. Hoang, C. Wang, J. F. Kang, J. H. Ahn, Y. Chai, *Nat. Electron.* **2022**, *5*, 84.
- [51] B. S. Ouyang, J. L. Wang, G. Zeng, J. M. Yan, Y. Zhou, X. X. Jiang, B. J. Shao, Y. Chai, *Nat. Electron.* **2024**, *7*, 705.
- [52] C. Feng, B. W. Li, Y. Dong, X. D. Chen, Y. Zheng, Z. H. Wang, H. B. Lin, W. Jiang, S. C. Zhang, C. W. Zou, G. C. Guo, F. W. Sun, *Sci. Adv.* **2023**, *9*, adg9376.
- [53] G. Li, D. G. Xie, Z. Y. Zhang, Q. L. Zhou, H. Zhong, H. Ni, J. O. Wang, E. J. Guo, M. He, C. Wang, G. Z. Yang, K. J. Jin, C. Ge, *Adv. Funct. Mater.* **2022**, *32*, 2203074.
- [54] R. Yuan, Q. Duan, P. J. Tiw, G. Li, Z. Xiao, Z. Jing, K. Yang, C. Liu, C. Ge, R. Huang, Y. Yang, *Nat. Commun.* **2022**, *13*, 3973.
- [55] M. Kumar, S. Lim, J. Kim, H. Seo, *Adv. Mater.* **2023**, *35*, 2210907.
- [56] O. Krestinskaya, K. N. Salama, A. P. James, *IEEE Transactions on Circuits and Systems I: Regular Papers*, IEEE, **2019**, *66*, 719.
- [57] M. Giordano, G. Cristiano, K. Ishibashi, S. Ambrogio, H. Tsai, G. W. Burr, P. Narayanan, *IEEE J. Emerg. Sel. Top. Circuits Syst.* **2019**, *9*, 367.
- [58] J. T. Fu, C. B. Nie, F. Y. Sun, G. L. Li, H. F. Shi, X. Z. Wei, *Sci. Adv.* **2024**, *10*, adk8199.
- [59] C. Y. Wang, S. J. Liang, S. Wang, P. Wang, Z. Li, Z. Wang, A. Gao, C. Pan, C. Liu, J. Liu, H. Yang, X. Liu, W. Song, C. Wang, B. Cheng, X. Wang, K. Chen, Z. Wang, K. Watanabe, T. Taniguchi, J. J. Yang, F. Miao, *Sci. Adv.* **2020**, *6*, aba6173.
- [60] X. Zhang, Y. Zhuo, Q. Luo, Z. Wu, R. Midya, Z. Wang, W. Song, R. Wang, N. K. Upadhyay, Y. Fang, F. Kiani, M. Rao, Y. Yang, Q. Xia, Q. Liu, M. Liu, J. J. Yang, *Nat. Commun.* **2020**, *11*, 51.
- [61] J. Del Valle, P. Salev, F. Tesler, N. M. Vargas, Y. Kalcheim, P. Wang, J. Trastoy, M. H. Lee, G. Kassabian, J. G. Ramirez, M. J. Rozenberg, I. K. Schuller, *Nature* **2019**, *569*, 388.
- [62] L. L. Chen, Y. Y. Cui, H. J. Luo, Y. F. Gao, *RSC Adv.* **2020**, *10*, 18543.
- [63] L. S. Kalman, E. M. Bassett, *P. Soc. Photo-Opt. Ins.* **1997**, *3118*, 57.
- [64] J. Li, J. M. Bioucas-Dias, A. Plaza, *IEEE T. Geosci. Remote* **2010**, *48*, 4085.
- [65] J. Du, W. S. Li, K. Lu, B. Xiao, *Neurocomputing* **2016**, *215*, 3.
- [66] Z. Zhou, M. A. Chia, S. K. Wagner, M. S. Ayhan, D. J. Williamson, R. R. Struyven, T. Liu, M. Xu, M. G. Lozano, P. Woodward-Court, Y. Kihara, U. K. B. Eye, C. Vision, A. Altmann, A. Y. Lee, E. J. Topol, A. K. Denniston, D. C. Alexander, P. A. Keane, *Nature* **2023**, *622*, 156.
- [67] J. Staal, M. D. Abramoff, M. Niemeijer, M. A. Viergever, B. van Ginneken, *IEEE Trans. Med. Imaging* **2004**, *23*, 501.
- [68] J. Ordóñez-Miranda, Y. Ezzahri, K. Joulain, J. Drevillon, J. J. Alvarado-Gil, *Phys. Rev. B* **2018**, *98*, 075144.
- [69] O. Svensk, S. Suihkonen, T. Lang, H. Lipsanen, M. Sopanen, M. A. Odnoblyudov, V. E. Bougrov, *J. Cryst. Growth* **2007**, *298*, 811.
- [70] Z. Yang, C. H. Ko, V. Balakrishnan, G. Gopalakrishnan, S. Ramanathan, *Phys. Rev. B* **2010**, *82*, 205101.
- [71] K. Liu, C. Wang, K. Zhang, X. H. Ma, J. C. Bai, X. F. Zheng, A. Li, Y. Hao, *J. Appl. Phys.* **2024**, *135*, 144501.
- [72] G. Kresse, D. Joubert, *Phys. Rev. B* **1999**, *59*, 1758.
- [73] J. P. Perdew, K. Burke, M. Ernzerhof, *Phys. Rev. Lett.* **1997**, *78*, 1396.
- [74] G. Kresse, J. Furthmüller, *Phys. Rev. B* **1996**, *54*, 11169.
- [75] J. Zhuang, *arXiv preprint arXiv:1810.07810*, **2018**.
- [76] LARXEL, Med-MNIST, <https://www.kaggle.com/datasets/andrewmvd/medical-mnist>, **2020**, *4*.